TiO$_2$ nanotube arrays decorated with Au and Bi$_2$S$_3$ nanoparticles for efficient Fe^{3+} ions detection and dye photocatalytic degradation

Jianying Huang [1], Jiali Shen [1,2], Shuhui Li [1,3], Jingsheng Cai [2], Shanchi Wang [2], Yao Lu [3], Jihuan He [2], Claire J. Carmalt [3], Ivan P. Parkin [3], Yuekun Lai [1*]

[1] *College of Chemical Engineering, Fuzhou University, Fuzhou 350116, PR China*

[2] *National Engineering Laboratory for Modern Silk, College of Textile and Clothing Engineering, Soochow University, Suzhou 215123, PR China*

[3] *Materials Chemistry Research Centre, Department of Chemistry, University College London, London, UK*

* Corresponding author. Prof. Yuekun Lai; Tel.: +86 59122865220.

E-mail address: yklai@fzu.edu.cn (Y.K. Lai)

Due to increasingly serious environmental problems, many researchers are investigating green clean-energy to solve the world's energy supply issues. So a strategy that Au nanoparticles (Au NPs) and bismuth sulfide (Bi$_2$S$_3$) NPs are used to evenly decorate TiO$_2$ nanotube arrays (TiO$_2$ NTAs) was carried out. Composite materials demonstrated enhanced solar light absorption ability and excellent photoelectrochemical performance. This was attributed to the presence of Bi$_2$S$_3$ NPs with a narrow band gap and the decoration with noble metallic Au NPs which resulted in local surface plasmon resonance (LSPR) effects. The Au/Bi$_2$S$_3$@TiO$_2$ NTAs composites exhibit improved photocatalytic activity for the degradation of methylene blue (MB) under irradiation of UV and visible light. Moreover, the Au/Bi$_2$S$_3$@TiO$_2$ NTAs exhibits high fluorescence emission at 822 nm. Due to the better binding affinity between Bi$_2$S$_3$, TiO$_2$ and Fe^{3+} ions, the synthesized nanocomposites exhibit high selectivity to Fe^{3+} ions. The number of binding sites for Au/Bi$_2$S$_3$@TiO$_2$ NTAs was estimated to be 1.41 according to the double logarithmic regression method. The calculated value of "K" was 1862 M^{-1}. Fluorescence emission intensity decreases with increasing concentration (30 μM to 5000 μM). The detection limit of the synthesized sensor is 0.221 μM.

Key words: TiO$_2$ nanotube; Au; Bi$_2$S$_3$; Photocatalysis; Fluorescence sensing

1. Introduction

Green and clean energy demand has now become a mainstream trend due to environmental pollution and global energy crisis problems. Photocatalytic semiconductors have attracted wide attention as a promising strategy for solving these problems. Many researchers have developed nanostructured materials for the degradation of contaminants. Titanium dioxide (TiO_2) is widely studied due to its good photocatalytic activity, environmental safety, relatively low cost, mechanical stability and corrosion resistance[1-6]. It has been widely applied in many fields including photocatalytic degradation of contaminants, dye-sensitized solar cells, water splitting, gas sensors and biomedical materials[7-13]. However, TiO_2 nanotube arrays (TiO_2 NTAs) have some shortcomings, limiting their applications in many aspects[14-19]. TiO_2 has a wide band gap, which absorbs only 3-5% of the solar energy ($\lambda < 387$ nm), which gives low utilization rate[1]. Moreover, the separation of electrons-holes of TiO_2 NTAs is low resulting in a low photocatalytic activity.

A series of modification strategies have been carried out to overcome these disadvantages, such as anatase TiO_2 NTAs doped with metal, non-metal or semiconductor. Narrow bandgap semiconductors in particular bismuth-based semiconductors have been used to make TiO_2 NTAs susceptible to visible, maintain excellent charge transfer and photofluorescence properties[20]. So Bi_2S_3 have attracted considerable attention. Bi_2S_3 is a non-toxic photoconductive semiconductor material with nonlinear optical response and a narrow band gap (1.3 eV)[21]. As the conduction band (CB) energy level of Bi_2S_3 is 0.26 eV higher than that of TiO_2, the photogenerated electron can be shifted from Bi_2S_3 to TiO_2. In contrast, the valence band (VB) of TiO_2 is lower than the Bi_2S_3 one, so that the photogenerated hole can be shifted to Bi_2S_3. Hence, valid charge separation of electrons-holes in TiO_2 and Bi_2S_3 is possible[22,23]. Noble metal nanoparticles (Ag, Cu, Pt, Au etc.) dispersed on the surface of TiO_2 NTAs can enhance the capture of photo-generated electrons, accelerate the separation of electrons-holes, and thus inhibit photo-generated electrons-holes recombination[24-27]. The addition of Au NPs to TiO_2 can reduce the intermittent rate of the trap state and partially compensate for the negative effects of the surface trap sites, thereby improving the light conversion efficiency[28-30].

While addressing environmental energy issues, we must also pay attention to human health issues. Lots of transition metal ions, such as Cu^{2+}, Mn^{2+}, Ni^{2+}, Co^{2+}, Mo^{2+},

Fe^{3+}, Zn^{2+}, etc., are beneficial to body function. Among these, Fe^{3+} ion is one of the most dominant and abundant in the earth[31]. Fe^{3+} ions play a crucial role in many physiological and pathological processes such as enzyme catalysis, oxygen metabolism, electron transfer, RNA and DNA replication, blood production and thermoregulation[32]. Fluorescence sensing for metal ions is charming because it has the advantages of simplicity, affordability, high sensitivity, fast response and non-perturbative measurements, compared with spectrometric techniques[33]. Most of the current scientific works of fluorescent sensing are dedicated to detecting metal ions and other contaminants[34-36]. Fegley et al.[37] introduced the use of a fluorescent conjugated polymer as a chemical sensor to differentiate Fe^{2+} and Fe^{3+} ions. Wang et al.[38] reported a thiophene-modified rhodamine as a new turn-on fluorescent chemosensor to detect Fe^{3+} ions in aqueous media. Sheng et al.[39] reported a fluorescent probe for Fe^{3+} ions using a rhodamine derivative (RD1) with metal chelating moiety. The findings of these literature studies proved that fluorescence spectroscopy is the most popular method. Furthermore, as far as we know, most of the reported researches of induced Fe^{3+} ions are limited to dye-based biomolecule-based fluorescence, quantum dots, chelate-based sensors, etc.[40] It is rarely reported that Fe^{3+} ions are sensed by heterostructured Bi_2S_3 -TiO_2.

Herein, we developed a simple and effective method to produce $Au/Bi_2S_3@TiO_2$ NTAs composite. Au / Bi_2S_3 NPs composites were evenly distributed on TiO_2 NTAs surface. Au NPs functioned as electron trapping sites to enhance charge separation efficiency. Thus, $Au/Bi_2S_3@TiO_2$ NTAs heterogeneous composite was able to absorb solar light over a wide spectrum range because of the LSPR influence of Au and the narrow bandgap of Bi_2S_3. Compared to pure TiO_2 NTAs, the prepared $Au/Bi_2S_3@TiO_2$ NTAs composite exhibited superior photocatalytic activity under irradiation of the UV and visible light. In addition, it proved to act as an excellent fluorescent sensor, with good sensitivity, towards the detection of Fe^{3+} ions.

2. Experimental

2.1. Preparation of two-step anodized TiO2 NTAs

As shown in Scheme 1, the TiO_2 NTAs were constructed via a two-step anodization process. Specifically, titanium oxide was used as anode, a platinum sheet was used as cathode and NH_4F in ethylene glycol solution (0.5 wt% of NH_4F and 2 v%

of water in ethylene glycol) served as electrolytic solution. Before the anodization, the titanium foil (3.0 cm × 1.5 cm) was cleaned by ultrasonicating in 1 M sulfuric acid, acetone, and ethanol sequentially and rinsed by deionized water. The anodic oxidation was performed twice. The first anodic oxidation voltage was 55 V for 2 h, the second anodic oxidation voltage was 55 V for 8 min. The obtained TiO_2 NTAs were calcined in air at a temperature of 450 °C for 2 h to enhance the crystallographic form. The heating and cooling rate of calcination were both 5 °C min^{-1}. Anatase TiO_2 NTAs were obtained as a result of this final step.

2.2. Preparation of Au NPs

The solution of $HAuCl_4$ (0.005-0.02 wt%) dissolved in deionized water was put in an oil bath heated at 130 °C and stirred. At boiling, 600 g of deionized water containing 1.0 wt% of sodium citrate was rapidly added to the gold solution for a reaction time of 1, 2, 3, 4 hours. So four kinds of Au NPs reduced by sodium citrate were formed as shown in Scheme 1.

2.3. Preparation of Au NPs and Bi_2S_3 composites

According to Scheme 1, 50 ml of these four Au NPs solutions were successively measured out, then 500 μl of deionized water containing 3.0 mg of thioacetamide and 3.86 mg of bismuth acetate were added respectively, and the mixture was granted to react at 80 °C for 10 hours in the oven. Four mixed solutions of Au / Bi_2S_3 NPs was obtained where the concentration of Bi_2S_3 NPs remain unchanged.

2.4. Preparation of Au/Bi_2S_3@TiO_2 NTAs

According to Scheme 1, TiO_2 NTAs was added to 15 ml of an ethanol solution including 150 μl of 3-mercaptopropyltrimethoxysilane (MPTS) and 30 μl of NH_4OH (27%). The mixture was kept at room temperature in a dark room for 24 hours. The TiO_2 NTAs were rinsed with ethanol and deionized water. As prepared TiO_2 NTAs were immersed in 15 ml of Au/Bi_2S_3 NPs solution in the centrifuge tubes at 37 °C for 4 h in the oven.

2.5. Characterization

The morphology and structure of Au/Bi_2S_3@TiO_2 NTAs were measured by field emission scanning electron microscopy (FESEM, Hitachi-S4800). The microstructure and composition of the Au/Bi_2S_3 NPs were determined by utilizing a transmission electron microscope (TEM, FEI Tecnai G-20 operated at 200 kV). The crystal phases were employing an X-ray diffractometer (XRD) with Cu-Kα radiation (Philips, X′pert-Pro MRD). The elements were analysed by using an energy dispersive X-ray (EDX) spectrometer. Photoluminescence (PL) measurements were performed by utilizing fluorescence spectroscopy (HORIBA JOBIN YVON, FM4P-TCSPC) and xenon lamp as excitation sources (λex = 250 nm). The chemical state was studied by using X -ray photoelectron spectroscopy (XPS, KRATOS, Axis Ultra HAS). The binding energies were standardized with respects to C 1s peak at 284.5 eV. The UV-Vis diffuse reflectance spectra at 250-800 nm were measured by utilizing UV-3600 spectrophotometer.

2.6 Photoelectrochemical measurement

The electrochemical properties of Au/Bi_2S_3@TiO_2 NTAs electrodes were studied by CV measurements and chronoamperometry. The electrochemical experiments were carried out using a PGSTAT302N electrochemical workstation (Autolab, Switzerland). Prior to all measurements, the as-prepared electrodes were dip in phosphate buffer solution (pH = 7.2) for 15 min. TiO_2 NTAs or Au/Bi_2S_3@ TiO_2 NTAs used as working electrodes, Pt plates used as counter electrodes and Ag/AgCl used as reference electrodes in 0.1 M Na_2SO_4 aqueous solution in a standard three-electrode system. The working electrode was exposed to a xenon lamp (GY-10) at a distance of 15 cm. The intensity of light focused on the beaker was 100 mW/cm^2.

2.7 Photocatalytic measurement

The photocatalytic activity of 10 mg L^{-1} (pH = 8.5) MB contaminant solution was investigated by PS-GHX photochemical reactor. The UV and visible light sources were simulated by a mercury lamp (300 W) and a xenon lamp (300 W), respectively. The light source was 60 mm away from the quartz tube (the reactor). Before irradiation, all the electrodes were completely immersed in the 15 ml MB solution respectively in a quartz reactor in a dark room for 0.5 h to achieve adsorption-desorption equilibrium.

Under ambient conditions, MB concentration was measured at 463 nm by UV-Vis spectrophotometer (Hitachi, UV-1080, Japan).

2.8 Study of detection of metal ions

The prepared $Au/Bi_2S_3@TiO_2$ NTAs were soaked in different aqueous solutions, 10 mM of Cu^+, Al^{3+}, K^+, Pb^{2+}, Cu^{2+}, Fe^{3+}, Ni^{2+}, Cd^{2+}, NH_4^+, Mn^{2+} and Zn^{2+} for 1 h. Then, the samples were taken out and dried. The fluorescence spectra were measured at excitation wavelength 380 nm and emission wavelength 822 nm, respectively. To study the selectivity of the composites for Fe^{3+} ions, interference experiments were studied by mingling other metal ion solutions with a constant concentration (300 M) of Fe^{3+} ions solutions.

3. Results and Discussion

Fig. 1 exhibits the SEM images of TiO_2 NTAs loaded with Au/Bi_2S_3 NPs mixed together (a), only Au (b) and Bi_2S_3 (c) TiO_2 NTAs. It is possible to see that most of the Au/Bi_2S_3 NPs were on the surface of the TiO_2 NTAs with a small amount of Au/Bi_2S_3 NPs also loaded into the TiO_2 NTAs structure as shown in Fig. 1(a). On the contrary, low loading of nanoparticles was found in TiO_2 NTAs sample loaded only with Au (Fig. 1(b)) or Bi_2S_3 (Fig. 1(c)). As shown in Fig. 1(d), the TiO_2 NTAs prepared by the two-step anodization method[41] have smooth surface and arranged order. The diameter of the tube is about 100 nm. Fig. S1(a, b) show 0.02 wt % and 0.005 wt % Au/Bi_2S_3 NPs decorating the TiO_2 NTAs for a reaction time of 2 h. Fig. S1(a, b) indicate that loading of Au/Bi_2S_3 NPs was not uniform at higher concentrations of Au NPs.

Fig. 2(a, b) show most of the Au/Bi_2S_3 NPs was on the surface of the TiO_2 NTAs with a small amount of Au/Bi_2S_3 NPs also loaded into the TiO_2 NTAs structure. Fig. 2(c) shows the EDX spectra of $Au/Bi_2S_3@TiO_2$ NTAs. It was found that the elements of the sample included Ti, O, Au, Bi, and S, and their atomic percentages were 34.62%, 64.49%, 0.09%, 0.30%, and 0.51% respectively. Fig. 2(d) displays the area mapping of the elements. The relatively even colours in the images indicate that the distribution of Au, Bi, and S is uniform.

The TEM images, Fig. 3(a, b), further show that the Au/Bi_2S_3 NPs were uniformly distributed on the outside and inside of the TiO_2 NTAs. The high resolution transmission electron microscope (HRTEM) (Fig. 3(c)) and selected area EDX

6

mapping (Fig. 3(d)) show that the lattice spacing of the TiO_2 anatase (101) plane is 0.35 nm, Au (111) plane spacing is 0.237 nm, and the interplanar spacing of Bi_2S_3 (130) is 0.36 nm[22]. As shown in Fig. S2(a), the size of Au/Bi_2S_3 NPs were about 15 nm and 20 nm, respectively. HRTEM images show that the Au/Bi_2S_3 NPs were both dispersed and combined as shown in Fig. S2(b-d).

XPS measurements were implemented so as to study the chemical composition and elemental valence state of Au/Bi_2S_3 NPs on the TiO_2 NTAs. The XPS spectra (Fig. 4(a)) confirmed the presence of Au, Bi, S, C, O, and Ti. The binding energy peaks at 284.5 eV, 458.9 eV, and 532.4 eV refer to C 1s, Ti 2p, and O 1s, respectively[42,43]. Fig. 4(b-d) exhibited the higher resolution XPS spectra of Au 4f, Bi 4f and S 2p core level for $Au/Bi_2S_3@TiO_2$ NTAs. The binding energies of 83.8 eV (Au $4f_{7/2}$) and 87.2 eV (Au $4f_{5/2}$) were found in the XPS spectrum (Fig. 4(b)), which indicates the existence of elemental Au NPs[44]. The two strong peaks at 157.8 eV (Bi $4f_{7/2}$) and 163.2 eV (Bi $4f_{5/2}$) in Fig. 4(c) correspond to the standard Bi^{3+} peaks of Bi_2S_3[45]. The XPS spectrum of sulphur was fitted into two peaks located at 159.2 eV and 164.3 eV shown in Fig. 4(d), which are designated to S $2p_{3/2}$ and $2p_{1/2}$ and correspond to those expected for a sulphide anion. Now, the as-synthesized Bi_2S_3 and Au were confirmed by XPS analysis.

XRD measurements were utilized to characterize the crystal phases of the pure TiO_2 NTAs, $Au/Bi_2S_3@TiO_2$ NTAs, $Au@TiO_2$ NTAs and $Bi_2S_3@TiO_2$ NTAs. As shown in Fig. S3, all diffraction peaks were ascribed to TiO_2. The diffraction peaks at 25.3°, 37.9°, 48.0° and 53.9° of pure TiO_2 NTAs correspond to the (101), (004), (200) and (105) planes of the TiO_2 anatase phase (JCPDS no. 21-1272) indicating the formation of anatase TiO_2 after annealing at 450 °C for 3 h. However, no obvious peaks of Bi_2S_3 and Au were observed in the $Au/Bi_2S_3@TiO_2$ NTAs, probably due to the smaller size and well dispersion of Bi_2S_3/Au NPs.

The photocurrent intensity test was performed in simulated sunlight. The switch was turned on and off alternately every 30 seconds to analyze the photo-induced charge separation. The short-lived photocurrent responses of pure TiO_2 NTAs and $Au/Bi_2S_3@TiO_2$ NTAs were measured with or without visible light by chronoamperometry. The photocurrent density of all samples raised when the light was on, and reduced when the light was off. The photocurrent density of all samples will fall closer to zero in the absence of light irradiation. Measured photocurrent densities of 0.01 wt% $Au/Bi_2S_3@TiO_2$ NTAs, pristine TiO_2 NTAs, $Au@TiO_2$ NTAs and $Bi_2S_3@TiO_2$ NTAs were 0.75, 0.3, 0.5, 0.6 mA/cm^2 shown in Fig. 5(a) while those of

0.02, 0.01, 0.005 wt% Au/Bi$_2$S$_3$@TiO$_2$ NTAs were 0.7, 0.75, 0.45 mA/cm^2, respectively (Fig. S4(a)). The higher responsive photocurrent of Au/Bi$_2$S$_3$@TiO$_2$ NTAs may be ascribed to two reasons: the sensitization of Au/Bi$_2$S$_3$ NPs significantly extends the response of TiO$_2$ NTAs into the visible region. In addition, the high separation rate of photo-generated electrons-holes could promote the separation and shift of photo-generated electrons[46,47].

Fig. 5(b) shows the photo luminescence emission spectra of the 0.01 wt% Au/Bi$_2$S$_3$@TiO$_2$ NTAs, Au@TiO$_2$ NTAs, Bi$_2$S$_3$@TiO$_2$ NTAs and pure TiO$_2$ NTAs catalysts under excitation of 380 nm UV light. Compared to TiO$_2$ with or without Au or Bi$_2$S$_3$, the Au/Bi$_2$S$_3$@TiO$_2$ NTAs shows a decrease in photo luminescence intensity indicating a lower electrons-holes recombination rate on Au/Bi$_2$S$_3$@TiO$_2$ NTAs catalyst. This is consistent with literature that photo-generated electrons shift from the CB of TiO$_2$ to Au NPs, which leads to the separation of electrons and holes leading to a higher photocatalytic activity when Au/Bi$_2$S$_3$@TiO$_2$ NTAs is used as the catalysts[48,49]. Fig. S4(b) shows the low fluorescence intensity of different concentrations of Au NPs of Au/Bi$_2$S$_3$@TiO$_2$ NTAs which also indicates a lower electrons-holes recombination rate. As shown in Fig. 5(c), the optical absorption performance of the prepared photocatalyst (200 nm-800 nm) was investigated using UV-Vis diffuse reflectance spectroscopy. The strong enhanced absorption from 400 to 600 nm can be attributed to the LSPR of Au NPs. Compared to the pristine TiO$_2$ NTAs, Au/Bi$_2$S$_3$@TiO$_2$ NTAs enhanced the photoelectric conversion quantum yield. As the concentration of the precursor increases, the absorption of the Au/Bi$_2$S$_3$@TiO$_2$ NTAs increases. However, the precursor concentration increased again leading to a decrease in the relative absorption intensity in the Au/Bi$_2$S$_3$@TiO$_2$ NTAs electrode (Fig. S4(c)). The relative adsorption value of 0.01 wt% Au/Bi$_2$S$_3$@TiO$_2$ NTAs sample in visible spectrum is the best, which is consistent with the response of photocurrent.

The photocatalytic activity of the as-obtained Au/Bi$_2$S$_3$@TiO$_2$ heterostructure was investigated by UV and simulated visible light photo-degradation of MB dye as representative waste water contaminant. Prior to the photocatalytic reaction, the photocatalyst required an adsorption-desorption experiment to achieve an adsorption-desorption equilibrium balance and we found that the sample reached equilibrium after 1 h. Fig. 6(a, b) show the degradation rate of MB under UV and visible light irradiation, respectively. Distinctively the degradation rate of MB by using the pristine TiO$_2$ NTAs electrode shows just about 10.5% with UV light irradiation for 120 min (Fig. 6(a)). But
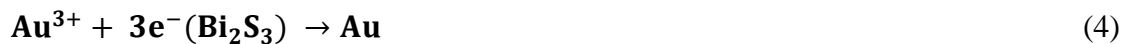
the photocatalytic activity was improved due to the decoration of Au/Bi_2S_3 NPs with a degradation rate of approximately 70%. By contrast, the degradation rate of Au@TiO_2 NTAs and Bi_2S_3@TiO_2 NTAs electrodes were only about 45% and 62% under the same condition. When the light source became simulated visible light (Fig. 6(b)), the MB exhibited about 38% degradation after 120 min for the pristine TiO_2 NTAs electrode. The degradation of MB for the Au/Bi_2S_3@TiO_2 NTAs electrode was 60%, which is lower than that under the UV light[50,51].

In order to evaluate the stability of the Au/Bi_2S_3@TiO_2 NTAs electrode, four cycles of photocatalytic degradation of contaminants were carried out under the same environment. The last degradation efficiency of the Au/Bi_2S_3@TiO_2 NTAs electrode under UV and visible light exposure did not display any significant deviation shown in Fig. 7(a, b), which indicates the stability of the electrode.

In order to further understand the catalytic mechanism, we performed a free radical capture experiment. The influences of several radical scavengers on the photocatalytic degradation of MB were detected. Ammonium oxalate (AO), isopropanol (IPA) and 1, 4-benzoquinone (BQ) served as h^+, ·OH and O_2^- scavengers respectively in the reaction system. As shown in Fig. 7(c), when BQ was added, the degradation efficiency was high in the absence of the action of O_2^-, and thus O_2^- plays a secondary role. Similarly, when AO and IPA were added, the degradation effect was significantly reduced, indicating that ·OH and h^+ play a major role during photocatalytic degradation.

Due to the high electron affinity of Au, we propose that the interface between Bi_2S_3/Au NPs formed a Schottky junction, and the electric field of the Schottky junction was enhanced to promote the separation of electrons-holes. A schematic synergetic mechanism of MB photodegradation is illustrated in Scheme 2A. The surface of the photogenerated electrons can react with the absorbed oxygen molecules, resulting in O_2^-. Bi_2S_3 surface can also absorb H_2O molecules to produce ·OH. Another part of the enhanced photocatalytic activity is that the n-type TiO_2 is close to CB, and the Fermi level of the Bi_2S_3 and TiO_2 form a p-n heterojunction[52,53], and the Fermi level of the p-type Bi_2S_3 is close to VB. When the n-type TiO_2 and the p-type Bi_2S_3 form a p-n heterojunction, it generates an internal electric field between the surface of TiO_2 and Bi_2S_3. The electrons are transferred from Bi_2S_3 to TiO_2, and the holes are transferred from TiO_2 to Bi_2S_3 until the system reaches equilibrium. Under irradiation with UV, the surface of the n-type TiO_2 produces photo-generated electron

holes drifting in the different direction of the electric field. The holes transfer to the negative field, when the electrons flow to the positive field. Hence the electrons move from the CB of Bi_2S_3 to the CB of TiO_2, and accordingly, the holes move from the VB of TiO_2 to the VB of Bi_2S_3. So the reduction of electrons-holes recombination is reduced[54]. The photocatalytic degradation mechanism of MB is following:

$$Bi_2S_3 + h\upsilon \rightarrow Bi_2S_3\ (e^- + h^+) \tag{1}$$

$$Bi_2S_3(e^-) + TiO_2 \rightarrow TiO_2(e^-) + Bi_2S_3 \tag{2}$$

$$Au + h\upsilon \rightarrow Au^{3+} + 3e^-(TiO_2) \tag{3}$$

$$Au^{3+} + 3e^-(Bi_2S_3)\ \rightarrow Au \tag{4}$$

$$TiO_2(e^-) + O_2 \rightarrow TiO_2 + \cdot O_2^- \tag{5}$$

$$\cdot O_2^- + H_2O \rightarrow HO_2 \cdot + OH^- \tag{6}$$

$$Bi_2S_3(h^+) + OH^- \rightarrow OH \cdot + Bi_2S_3 \tag{7}$$

$$OH \cdot + MB \rightarrow Degradation \tag{8}$$

Recently, heavy attention to environmental protection and human health has urged active research on the underlying effects of transition metal ions. Therefore, scientists have made tremendous efforts to synthesize effective sensors for detecting transition metal ion[55-62]. In our sensing experiment, the sample was immersed in solutions (10 mM) of different metal ions (Cu^+, Al^{3+}, K^+, Pb^{2+}, Cu^{2+}, Fe^{3+}, Ni^{2+}, Cd^{2+}, NH_4^+, Mn^{2+} and Zn^{2+}) for 1 hour to study the selectivity of the sample to metal ions. As can be seen in Fig. 8, Fe^{3+} ion has the highest fluorescence intensity change among the 11 kinds of the metal ions. Compared with other metal ions, the fluorescence quenching efficiency of Fe^{3+} ions is greatly improved which clearly demonstrates the high sensitivity and excellent selectivity of $Au/Bi_2S_3@TiO_2$ NTAs to Fe^{3+} ions.

UV-Vis spectroscopy is extensively used, and the characteristics of the absorption peak can be used for simple structural analysis. As shown in Fig. 9(a), the $Au/Bi_2S_3@TiO_2$ NTAs with different Fe^{3+} ions concentrations have obvious absorption peaks at 353 nm, and with the increase of Fe^{3+} ions concentration, the absorption peaks are increasing. The increase indicates that the Fe^{3+} ions have strong interaction with the $Au/Bi_2S_3@TiO_2$ NTAs, further explaining that the $Au/Bi_2S_3@TiO_2$ NTAs and Fe^{3+} ions are formed by the ground state complex, which results from the surface of the $Au/Bi_2S_3@TiO_2$ NTAs absorbed by Fe^{3+} ions[63,64]. As can be seen from Fig. 9(b), the fluorescence intensity of the $Au/Bi_2S_3@TiO_2$ NTAs is affected by the concentration of Fe^{3+} ions, and as the concentration of Fe^{3+} ions increases, the fluorescence intensity

decreases. There is a linear relationship between them as shown in Fig. 10(a). When the Fe^{3+} ions concentration is beyond 0.01 M, the fluorescence intensity is completely quenched. Therefore, it can be used to determine Fe^{3+} ions. In order to study whether the fluorescence response of Fe^{3+} ions is interfered in the presence of other metal ions, Cu^+, Al^{3+}, K^+, Pb^{2+}, Cu^{2+}, Fe^{3+}, Ni^{2+}, Cd^{2+}, NH_4^+, Mn^{2+} and Zn^{2+} are added to the $Au/Bi_2S_3@TiO_2$ NTAs/Fe^{3+} system, respectively. It can be seen from Fig. 9(c) that the fluorescence intensity of the $Au/Bi_2S_3@TiO_2$ NTAs and Fe^{3+} ions is substantially unchanged in the presence of other metals, indicating that the fluorescence sensor has no effect in detecting Fe^{3+} ions in a solution mixed with other metal ions. The pH of the solution also showed an effect on the fluorescence properties, so we investigated the influence of pH on the fluorescence response of $Au/Bi_2S_3@TiO_2$ NTAs by adjusting the pH of the solution while ensuring the same Fe^{3+} ions concentration. As can be seen from Fig. 9(d), the fluorescence intensity first increases with increasing pH and then decreases with increasing pH, so the optimum pH is 3.07.

The electron transfer process arouses the transition metal center to undergo fluorescence quenching[65]. The metal center Fe^{3+} ions have a half full level, and its energy must be between VB and CB of the fluorophore in order to realize electron transfer to achieve fluorescence quenching[40]. This is achieved by TiO_2 NTAs modified with Au/Bi_2S_3 NPs. Then two-electron exchange occurs, which transforms the fluorescent group into a matrix, resulting in non-radiative D-D decay in the metal center and fluorescence quenching, as shown in Scheme 2B.

Fluorescence quenching of the $Au/Bi_2S_3@TiO_2$ NTAs involves static quenching. The binding constants and the amount of binding sites were calculated by log $[(I_o-I)/I]$ versus log[C] double logistic regression curves (Fig. 10(b)). The formulas are as follows:

$$\text{Log}[\frac{I_0-I}{I}] = \log K + n\log \tag{9}$$

Where K is the binding constant and [C] is the concentration of the quencher agent. The amount of binding sites of the $Au/Bi_2S_3@TiO_2$ NTAs per Fe^{3+} ion was 1.41, and the calculated value of "K" was 1862 M^{-1}. The higher values of 'K' and 'n' demonstrate a preferable interaction of the $Au/Bi_2S_3@TiO_2$ NTAs and Fe^{3+} ions[66]. The detection limit is 0.221 μM according to this formula (3σ/S), which is much lower than the ones found in literature, as shown in Table 1[67-70]. Furthermore, the method of synthesizing fluorophores is simple and cheap compared to the previous methods[71-74].

4. Conclusions

In summary, a simple method was developed to prepare $Au/Bi_2S_3@TiO_2$ NTAs. Au/Bi_2S_3 NPs were evenly distributed on the TiO_2 NTAs. The presence of Au NPs has the function of electron traps which enhances the charge separation efficiency. $Au/Bi_2S_3@TiO_2$ NTAs composite exhibits effective visible light activation and good electron transfer ability due to the LSPR effect. Compared with the not functionalised TiO_2 NTAs, the prepared $Au/Bi_2S_3@TiO_2$ NTAs composite exhibits increased photocatalytic activity for the photo-degradation of MB under the irradiation of UV and visible light. Moreover, Au/Bi_2S_3 NPs are uniformly dispersed on TiO_2 NTAs, exhibiting high fluorescence emission at 822 nm. Due to the better binding affinity of Bi_2S_3, TiO_2 and Fe^{3+} ions, the synthesized nanocomposites show high selectivity to Fe^{3+} ions. The amount of binding sites of $Au/Bi_2S_3@TiO_2$ NTAs was estimated to be 1.41 from the double logarithmic regression method. The calculated value of "K" was 1862 M^{-1}. Fluorescence emission intensity decreases with increasing concentration (30 μM to 5000 μM). The best pH was 3.07. The detection limit of the synthesized sensor is 0.221 μM.

References

[1] M.Y. Wang, X.C. Pang, D.J. Zheng, Y.J. He, L. Sun, C.J. Lin, Z.Q. Lin, J. Mater. Chem. A 4 (2016) 7190-7199.

[2] T. Boningari, S.N.R. Inturi, M. Suidan, P.G.Smirniotis, J. Mater. Sci. Technol. 31 (2018) 1494-1502.

[3] M.Z. Ge, C.Y. Cao, S.H. Li, Y.X. Tang, L.N. Wang, N. Qi, J.Y. Huang, K.Q. Zhang, S.S. Al-Deyab, Y.K. Lai, Nanoscale 8 (2016) 5226-5234.

[4] C. Li, W.Y. Yang, Q. Li, J. Mater. Sci. Technol. 34 (2018) 969-975.

[5] J.C. Qiu, J.H. Li, S. Wang, B.J. Ma, S. Zhang, W.B. Guo, X.D. Zhang, W. Tang, Y.H. Sang, H. Liu, Small 12 (2016) 1770-1778.

[6] Z.H. Zhao, J. Tian, Y.H. Sang, A. Cabot, H. Liu, Adv. Mater. 27 (2015) 2557-2582.

[7] M.Y. Li, N. Yuan, Y.W. Tang, L. Pei, Y.D. Zhu, J.X. Liu, L.H. Bai, M.Y. Li, J. Mater. Sci. Technol. 35 (2019) 604-609.

[8] M.Y. Wang, J. Iocozzia, L. Sun, C.J. Lin, Z.Q. Lin, Energy Environ. Sci. 7 (2014) 2182-2202.

[9] T.H. Tan, J.A. Scott, Y.H. Ng, R.A. Taylor, K.F. Aguey-Zinsou, R. Amal, J. Catal. 352 (2017) 638-648.

[10] Y.Z. Chen, A.X. Li, Q. Li, X.M. Hou, L.N. Wang, Z.H. Huang, J. Mater. Sci. Technol. 34 (2018) 955-960.

[11] Y. Cheng, H. Yang, Y. Yang, J.Y. Huang, K. Wu, Z. Chen, X.Q. Wang, C.J. Lin, Y.K. Lai, J. Mater. Chem. B 6 (2018) 1862-1886.

[12] J.S. Cai, J.L. Shen, X.N. Zhang, Y.H. Ng, J.Y. Huang, W.X. Guo, C.J. Lin, Y.K. Lai, Small Methods 2 (2019) 1800184.

[13] T.T. Qian, X.P. Yin, J.H. Li, H.E. Nian, H. Xu, Y. Deng, X. Wang, J. Mater. Sci. Technol. 34 (2018) 1314-1322.

[14] X.N. Zhang, M.Z. Ge, J.N. Dong, J.Y. Huang, J.H. He, Y.K. Lai, ACS Sustainable Chem. Eng. 7 (2019) 558-568.

[15] Y.B. Liu, Q.F. Yao, X.J. Wu, T.K. Chen, Y. Ma, C.N. Ong, J.P. Xie, Nanoscale 8 (2016) 10145-10151.

[16] M.Z. Ge, C.Y. Cao, J.Y. Huang, S.H. Li, Z. Chen, K.Q. Zhang, S.S. Al-Deyab, Y.K. Lai, J. Mater. Chem. A 4 (2016) 6772-6801.

[17] M.Z. Ge, Q.S. Li, C.Y. Cao, J.Y. Huang, S.H. Li, S.N. Zhang, Z. Chen, K.Q. Zhang, S.S. Al-Deyab, Y.K. Lai, Adv. Sci. 4 (2017) 1600152.

[18] Y.Z. Chen, A.X. Li, M. Jin, L.N. Wang, Z.H. Huang, J. Mater. Sci. Technol. 33 (2017) 728-733.

[19] H.G. Zhu, N. Goswami, Q.F. Yao, T.K. Chen, Y.B. Liu, Q.F. Xu, D.Y. Chen, J.M. Lu, J.P. Xie, J. Mater. Chem. A 6 (2018) 1102-1108.

[20] Y.L. Wan, M.M. Han, L.M. Yu, J.H. Jia, G.W. Yi, RSC Adv. 5 (2015) 78902-78909.

[21] D. Han, M.H. Du, C.M. Dai, D.Y. Sun, S.Y. Chen, J. Mater. Chem. A 5 (2017) 6200-6210.

[22] S. Paul, S. Ghosh, D. Barman, S.K. De, Appl. Catal. B 219 (2017) 287-300.

[23] C.Z. Wei, L.F. Wang, L.Y. Dang, Q. Chen, Q.Y. Lu, F. Gao, Sci. Rep. 5 (2015) 10599.

[24] J.N. Dong, X.N. Zhang, J.Y. Huang, S.W. Gao, J.J. Mao, J.S. Cai, Z. Chen, S. Sathasivam, C.J. Carmalt, Y.K. Lai, Electrochem. Commun. 93 (2018) 152-157.

[25] N.T. Nguyen, I. Hwang, T. Kondo, T. Yanagishita, H. Masuda, P. Schmuki, Electrochem. Commun. 79 (2017) 46-50.

[26] J.S. Cai, J.Y. Huang, Y.K. Lai, J. Mater. Chem. A 5 (2017) 16412-16421.

[27] D. Bhattacharyya, P. Kumar, Y.R. Smith, S.K. Mohanty, M. Misra, J. Mater. Sci. Technol. 34 (2018) 905-913.

[28] P. Kar, S. Farsinezhad, N. Mahdi, Y. Zhang, U. Obuekwe, H. Sharma, J. Shen, N. Semagina, K. Shankar, Nano Res. 9 (2016) 3478-3493.

[29] M.Z. Ge, J.S. Cai, J. Iocozzia, C.Y. Cao, J.Y. Huang, X.N. Zhang, J.L. Shen, S.C. Wang, S.N. Zhang, K.Q. Zhang, Y.K. Lai, Z.Q. Lin, Int. J. Hydrogen Energy 42 (2017) 8418-8449.

[30] Y. Shiraishi, N. Yasumoto, J. Imai, H. Sakamoto, S. Tanaka, S. Ichikawa, B. Ohtani, T. Hirai, Nanoscale 9 (2017) 8349-8361.

[31] Z.X. Zhang, F. Li, C.Y. He, H.W. Ma, Y.T. Feng, Y.A. Zhang, M. Zhang, Sensors Actuat. B 255 (2018) 1878-1883.

[32] C. Qin, D. Troya, C. Shang, S. Hildreth, R. Helm, K. Xia, Environ. Sci. Technol. 49 (2015) 956-964.

[33] M. Faraz, A. Abbasi, F.K. Naqvi, N. Khare, R. Prasad, I. Barman, R. Pandey, Sensors Actuat. B 269 (2018) 195-202.

[34] P. Wang, B.L. Li, N.B. Li, H.Q. Luo, Spectrochim. Acta A 135 (2015) 198-202.

[35] B.L. Ma, S.Z. Wu, F. Zeng, Sensors Actuat. B 145 (2010) 451-456.

[36] S. Sharma, S.K. Mehta, S.K. Kansal, Sensors Actuat. B 243 (2017) 1148-1156.

[37] M.E.A. Fegley, T. Sandgren, J.L. Duffy-Matzner, A.T. Chen, W.E. Jones Jr, J. Polym. Sci. Poly. Chem. 53 (2015) 951-954.

[38] K.P. Wang, Y. Lei, S.J. Zhang, W.J. Zheng, J.P. Chen, S.J. Chen, Q. Zhang, Y.B. Zhang, Z.Q. Hu, Sensors Actuat. B 252 (2017) 1140-1145.

[39] H.J. Sheng, X.M. Meng, W.P. Ye, Y. Feng, H.T. Sheng, X. Wang, Q.X. Guo, Sensors Actuat. B 195 (2014) 534-539.

[40] A. Syal, D. Sud, Sensors Actuat. B 266 (2018) 1-8.

[41] J.H. Yun, Y.H. Ng, C.H. Ye, A.J. Mozer, G.G. Wallace, R. Amal, ACS Appl. Mater. Interfaces 3 (2011) 1585-1593.

[42] R.P. Panmand, Y.A. Sethi, R.S. Deokar, D.J. Late, H.M. Gholap, J. Baeg, B.B. Kale, RSC Adv. 6 (2016) 23508-23517.

[43] Q.Y. Wang, R.C. Jin, C.L. Yin, M.J. Wang, J.F. Wang, S.M. Gao, Sep. Purif. Tech. 172 (2017) 303-309.

[44] J.L. Yang, C.Y. Mou, Appl. Catal. B 231 (2018) 283-291.

[45] Y. Huang, G. Xie, S.P. Chen, S.L. Gao, J. Solid State Chem. 184 (2011) 502-508.

[46] S. Anwer, G. Bharath, S. Iqbal, H.M. Qian, T. Masood, K. Liao, W.J. Cantwell, J.T. Zhang, L.X. Zheng, Electrochim. Acta 283 (2018) 1095-1104.

[47] L. Shi, Z. Li, T.D. Dao, T. Nagaobc, Y. Yang, J. Mater. Chem. A 6 (2018) 12978-12984.

[48] R.M. Wang, G. Cheng, Z. Dai, J. Ding, Y.L. Liu, R. Chen, Chem. Eng. J. 327 (2017) 371-386.

[49] H. L. Li, X.Y. Wu, J. Wang, Y. Gao, L.Q. Li, K.M. Shih, Int. J. Hydrogen Energy 41 (2016) 8479-8488.

[50] A. Helal, F.A. Harraz, A.A. Ismail, T.M. Sami, I.A. Ibrahim, Appl. Catal. B 213 (2017) 18-27.

[51] R.P. Panmand, Y.A. Sethi, R.S. Deokar, D.J. Late, H.M. Gholap, J. Baeg, B.B. Kale, RSC Adv. 6 (2016) 23508-23517.

[52] M.Y. Wang, L. Sun, Z.Q. Lin, J.H. Cai, K.P. Xie, C.J. Lin, Energy Environ. Sci. 6 (2013) 1211-1220.

[53] M.Y. Wang, D.J. Zheng, M.D. Ye, C.C. Zhang, B.B. Xu, C.J. Lin, L. Sun, Z.Q. Lin, Small 11 (2015) 1436-1442.

[54] M.Y. Wang, B. Wang, F. Huang, Z.Q. Lin, Angew. Chem. Int. Edit. 2019, doi:10.1002/anie.201811709.

[55] V.K. Gupta, N. Mergu, L.K. Kumawat, Sensors Actuat. B 223 (2016) 101-113.

[56] S.H. Lee, J. Kumar, S.K. Tripathy, Langmuir 16 (2000) 10482-10489.

[57] K.M.K. Swamy, H.N. Kim, J.H. Soh, Y. Kim, S.J. Kim, J. Yoon, Chem. Commun. (2009) 1234-1236.

[58] Z. Zhang, W.Q. Li, Q.L. Zhao, M. Cheng, L. Xu, X.H. Fang, Biosens. Bioelectron. 59 (2014) 40-44.

[59] X.J. Meng, S.L. Li, W.B. Ma, J.L. Wang, Z.Y. Hu, D.L. Cao, Dyes Pigments 154 (2018) 194-198.

[60] H. Wu, Z.K. Zheng, Y.M. Tang, N.M. Huang, R. Amal, H.N. Lim, Y.H. Ng, Sustainable Mater. Technol. 18 (2018) e00075.

[61] C.Y. Foo, H.N. Lim, A. Pandikumar, N.M. Huang, Y.H. Ng, J. Hazard. Mater. 304 (2016) 400-408.

[62] I. Ibrahim, H.N. Lim, R.M. Zawawi, A.A.Tajudin, Y.H. Ng, H. Guo, N.M. Huang, J. Mater. Chem. B 6 (2018) 4551-4568.

[63] L.N. Xu, W. Mao, J.R. Huang, S.H. Li, K. Huang, M. Li, J.L. Xia, Q. Chen, Sensors Actuat. B 230 (2016) 54-60.

[64] C.F. Wan, Y.J. Chang, C.Y. Chien, Y.W. Sie, C.H. Hu, A.T. Wu, J. Lumin. 178 (2016) 115-120.

[65] V. Balzani, F. Scandola, Pure & App. Chern. 62 (1990) 1099-1102.

[66] Y.R. Du, N.Z. Song, X.J. Lv, B. Hu, W.H. Zhou, Q. Jia, Dyes Pigments 138 (2017) 15-22.

[67] Y. Kang, X.J. Zheng, L.P. Jin, J. Colloid Interf. Sci. 471 (2016) 1-6.

[68] Y.L. He, Z.H. Yu, J.L. He, H.R. Zhang, Y.L. Liu, B.F. Lei, Sensors Actuat. B 262 (2018) 228-235.

[69] H. Hamishehkar, B. Ghasemzadeh, A. Naseri, R. Salehi, F. Rasoulzadeh, Spectrochimica Acta A 150 (2015) 934-939.

[70] W.C. Ding, J.K. Xu, Y.P. Wen, J. Zhang, H.T. Liu, Z.X. Zhang, Anal. Chim. Acta 967 (2017) 78-84.

[71] S. Samanta, B.K. Datta, M. Boral, A. Nandan, G. Das, Analyst 141 (2016) 4388-4393.

[72] X.X. He, X.M. Wang, L. Zhang, G.Z. Fang, J.F. Liu, S. Wang, Sensors Actuat. B 271 (2018) 289-299.

[73] S. Swami, A. Agarwala, D. Behera, R. Shrivastava, Sensors Actuat. B 260 (2018) 1012-1017.

[74] P.A. More, G.S. Shankarling, Sensors Actuat. B 241 (2017) 552-559.
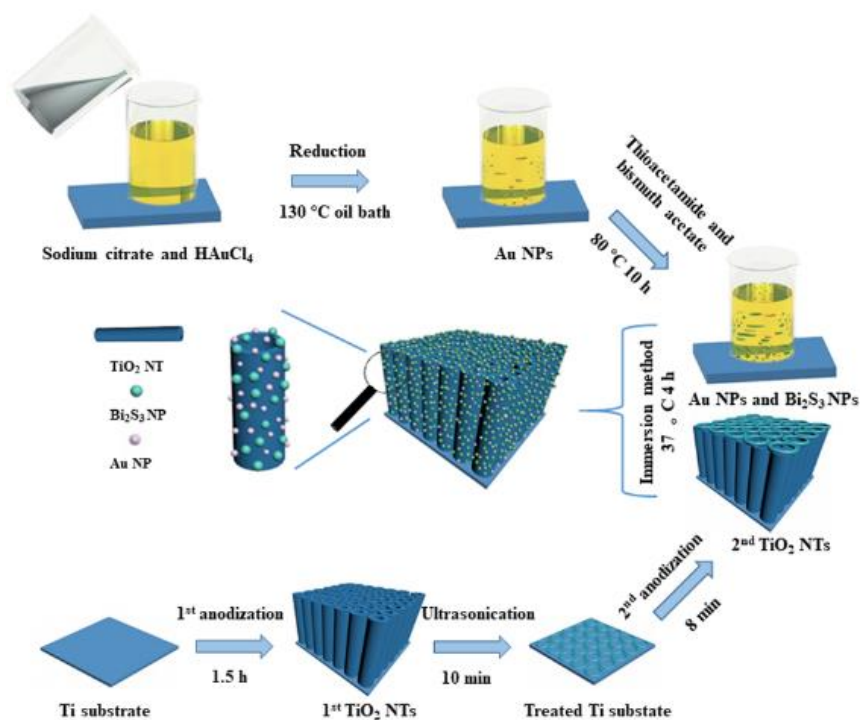
Scheme 1. Schematic illustration of the synthesis process for Au/Bi$_2$S$_3$@TiO$_2$ NTAs.
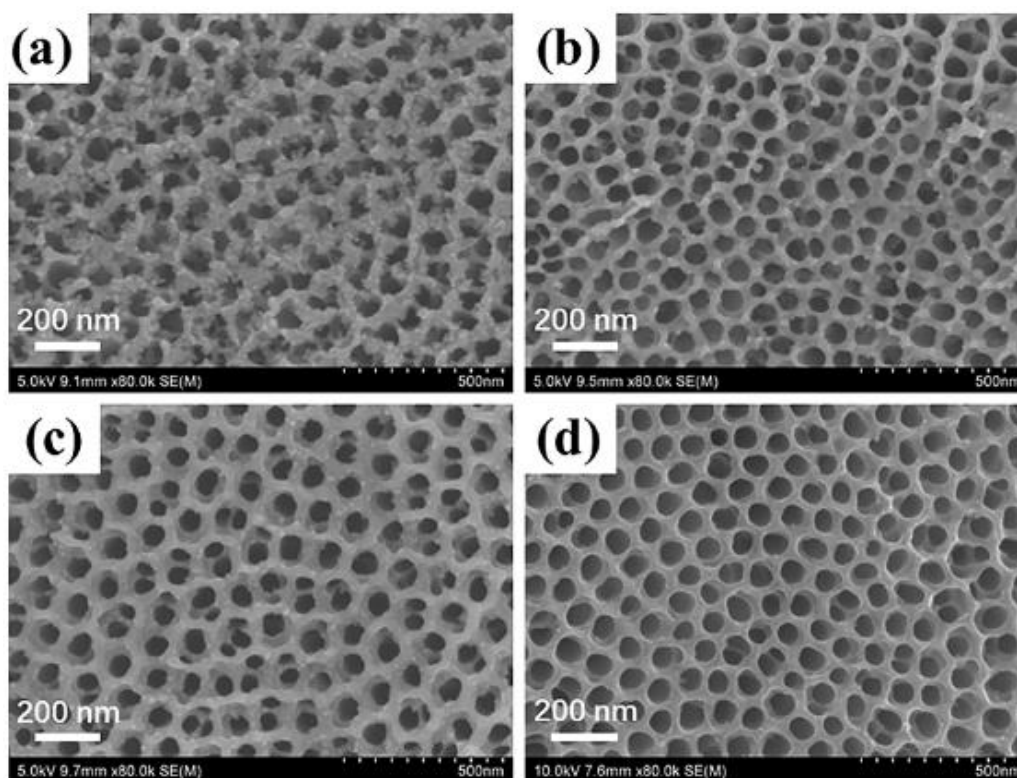
Figure 1. SEM images of 0.01 wt% Au/Bi$_2$S$_3$@TiO$_2$ NTAs (a), Au@TiO$_2$ NTAs (b),

Bi$_2$S$_3$@TiO$_2$ NTAs (c) and TiO$_2$ NTAs (d).

Element	Weight %	Weight % σ	Atomic %
Oxygen	37.023	0.481	64.487
Sulfur	0.581	0.070	0.505
Titanium	59.501	0.486	34.617
Gold	0.654	0.191	0.093
Bismuth	2.242	0.262	0.299
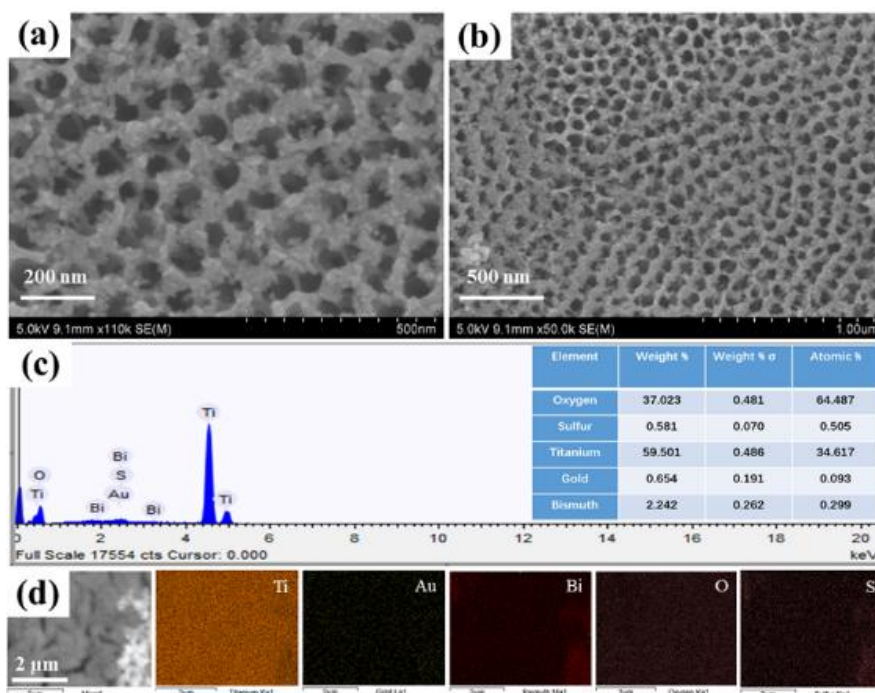
Figure 2. SEM images of 0.01 wt % $Au/Bi_2S_3@TiO_2$ NTAs in different magnifications (a, b). The corresponding EDX spectrum (c) and mapping (d) of $Au/Bi_2S_3@TiO_2$ NTAs.
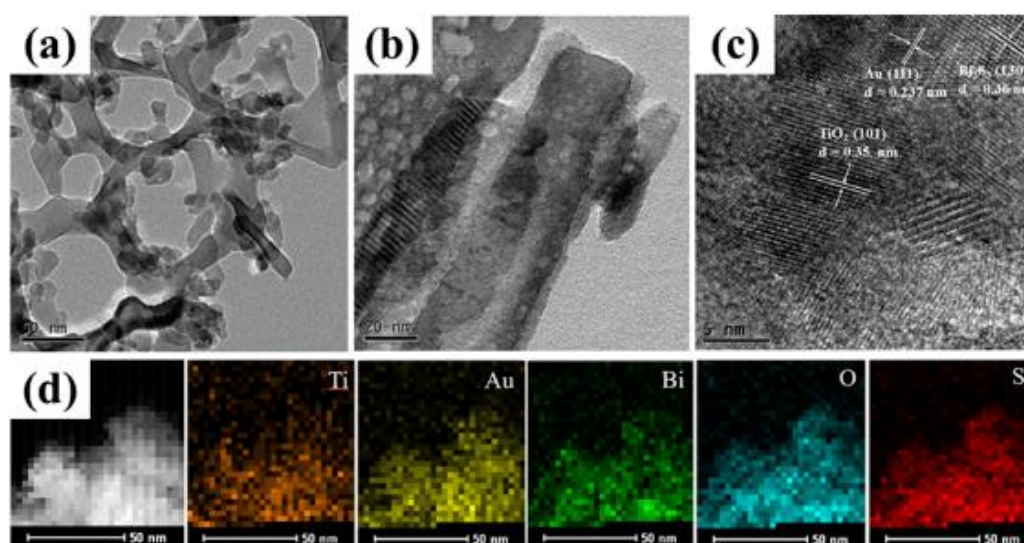
Figure 3. The TEM (a, b) and HRTEM (c) images of $Au/Bi_2S_3@TiO_2$ NTAs. Selected area EDX mapping (d) of the $Au/Bi_2S_3@TiO_2$ NTAs.
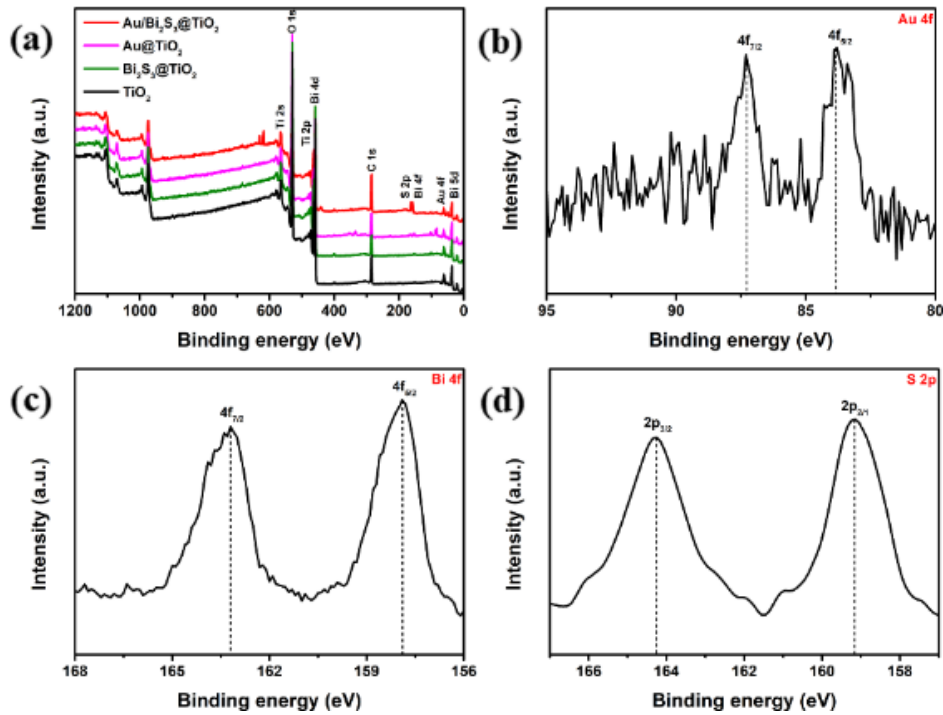
Figure 4. XPS spectra (a) and high resolution XPS spectra of Au 4f (b), Bi 4f (c) and S 2p (d) obtained on Au/Bi$_2$S$_3$@TiO$_2$ NTAs samples.
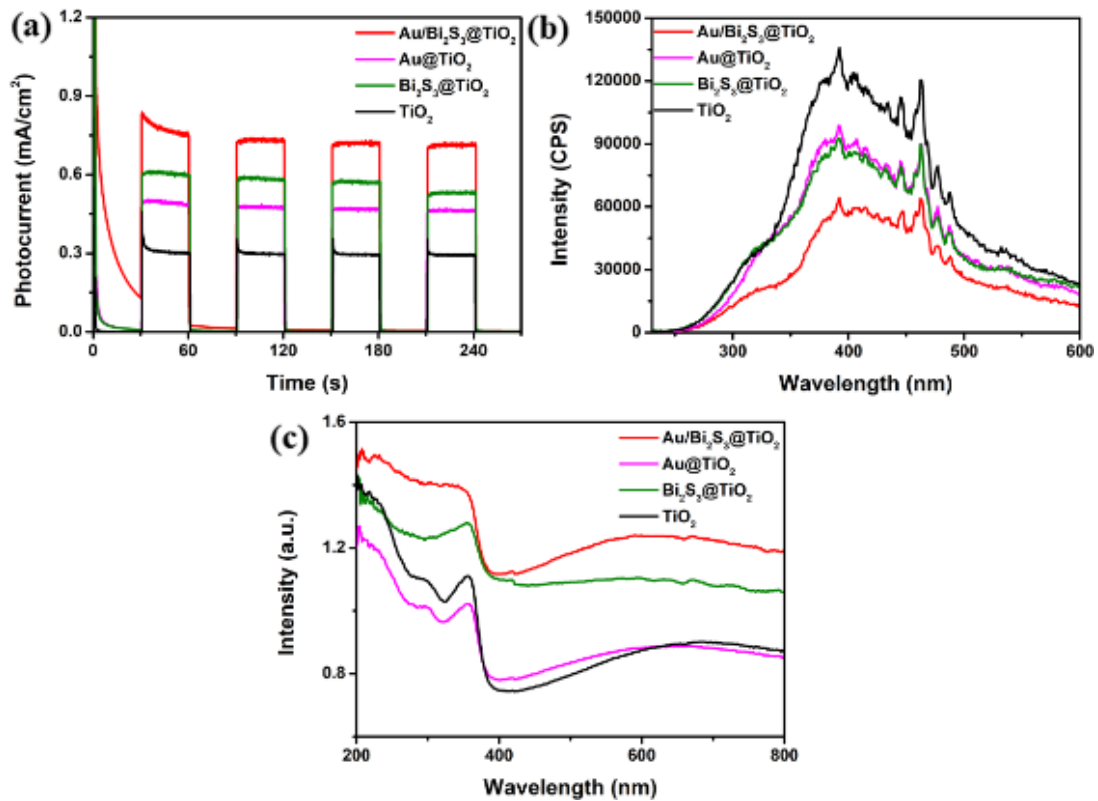
Figure 5. The samples of the photocurrent response (a), photofluorescence spectra excited at 380 nm (b), UV-Vis diffuse reflectance absorption spectra (c).
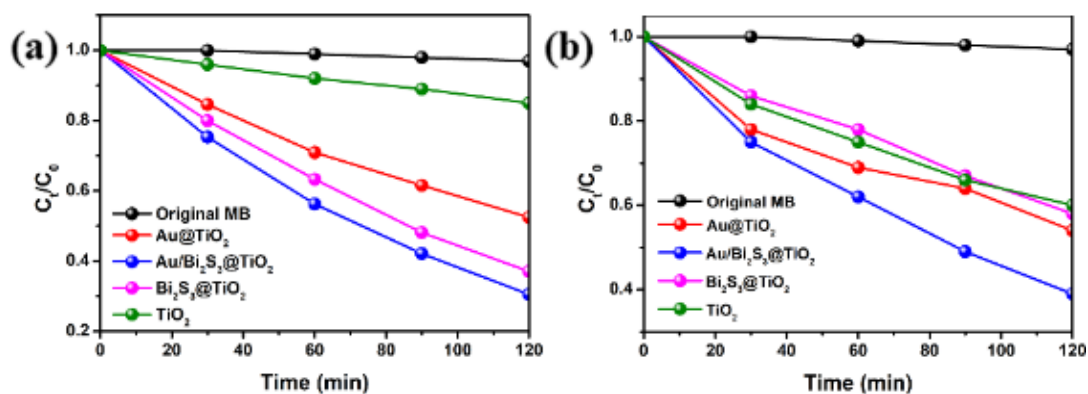
Figure 6. Degradation of MB under the UV light (a) and the visible light (b) irradiation for 120 min.
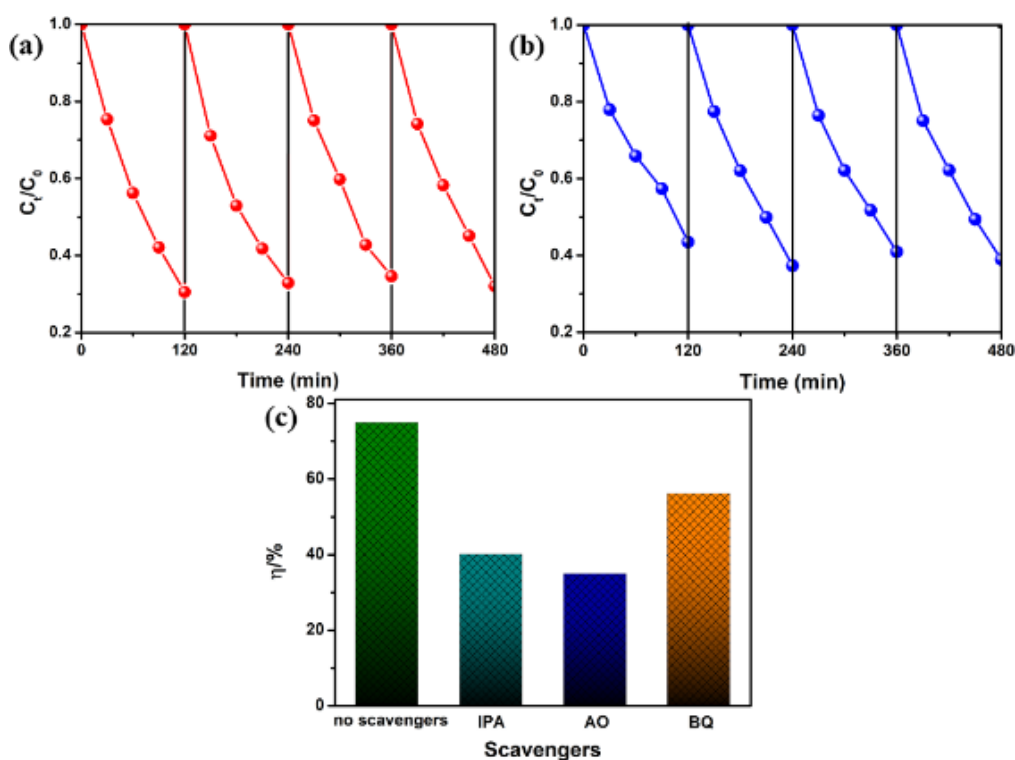
Figure 7. The reusability of Au/Bi$_2$S$_3$@TiO$_2$ NTAs under visible light (a) and UV (b) irradiation for 8 h. The influences of different scavengers (c) on the degradation of MB over Au/Bi$_2$S$_3$@TiO$_2$ NTAs.
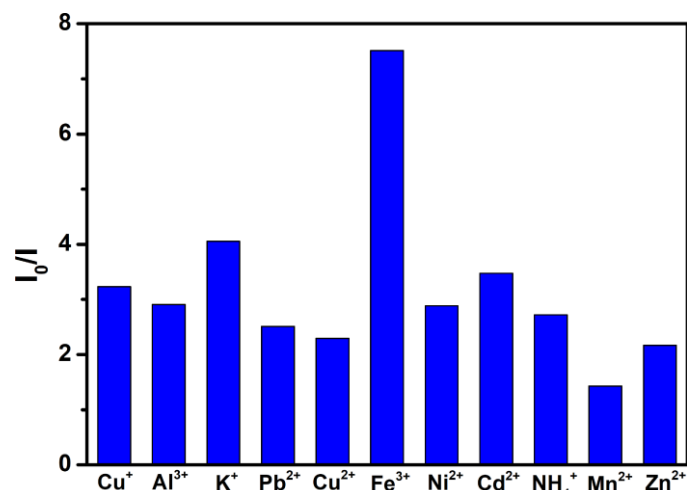
Figure 8. Fluorescence intensity changes (I_0/I) of the $Au/Bi_2S_3@TiO_2$ NTAs after being immersed into Cu^+, Al^{3+}, K^+, Pb^{2+}, Cu^{2+}, Fe^{3+}, Ni^{2+}, Cd^{2+}, NH_4^+, Mn^{2+} and Zn^{2+} aqueous solution.
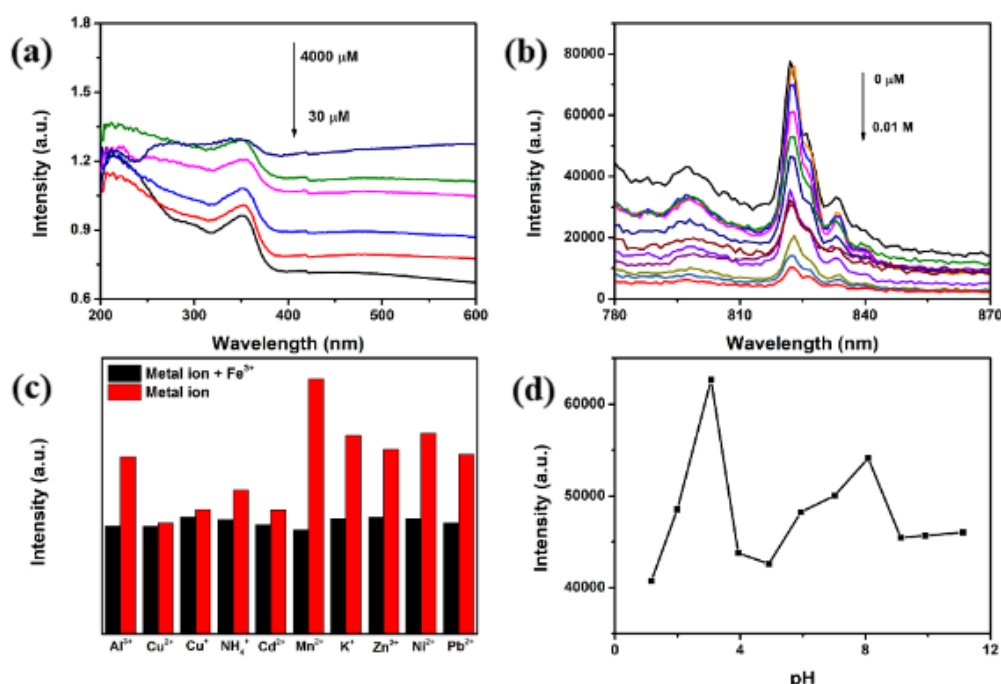
Figure 9. UV-Vis spectra of the $Au/Bi_2S_3@TiO_2$ NTAs with different concentrations of Fe^{3+} from 4000 µM to 30 µM (a). Fluorescence quenching of the $Au/Bi_2S_3@TiO_2$ NTAs with Fe^{3+} ions (0-400 mM) (b). Fluorescence response of the $Au/Bi_2S_3@TiO_2$ NTAs in the existence of 600 µM Fe^{3+} with/without multifarious metal ions in aqueous media (c). The fluorescence properties of the $Au/Bi_2S_3@TiO_2$ NTAs at different pH range (1-11) (d).
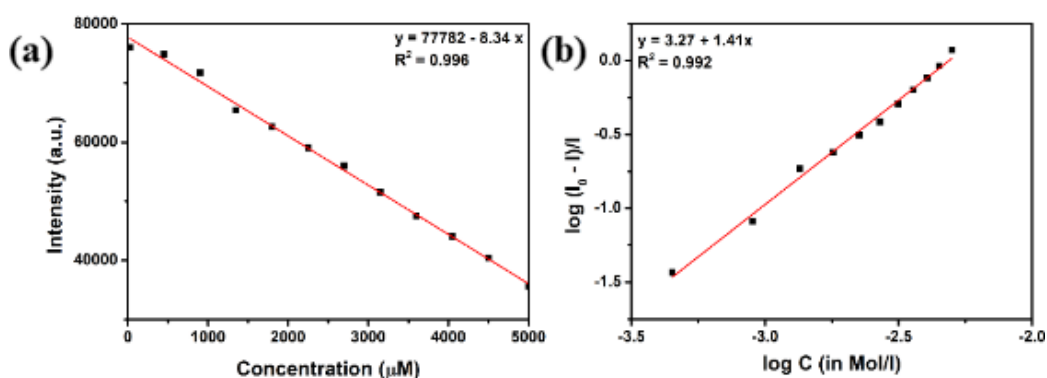
Figure 10. Linear relation (a) of the Au/Bi_2S_3@TiO_2 NTAs by adding different concentrations of Fe^{3+} when excited at 380 nm. Double logarithm regression plot (b) between log [(I_o - I)/I] versus log [C].

Table 1. The comparison of features of Fe^{3+} ions detection

Type of probe	Limit of detection	Method of synthesis	Reference
Eu-MOFs	45 µM	Heating method	67
Red emissive carbon dots	0.45µM	Solvothermal method	68
Water-soluble carbon dots	6.05 µM	Hydrothermal oxidation	69
Conjugated polymer thin film	5.3 µM	Direct electropolymerization	70
Au/Bi_2S_3@TiO_2 NTAs	0.221 µM	Soaking method	This work

22
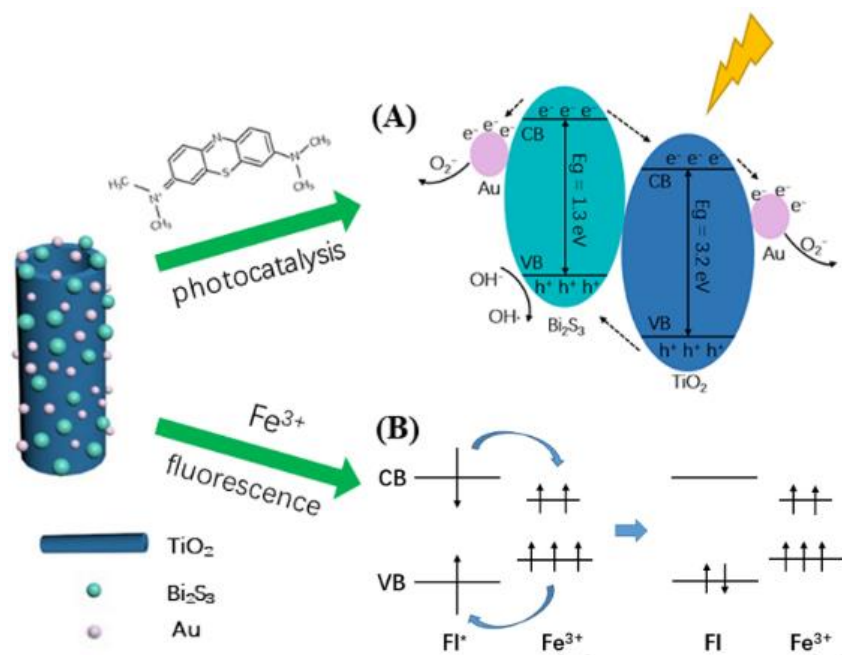
Scheme 2. The mechanism for MB photodegradation (A) and fluorescence detecting Fe^{3+} ions (B) over Au/Bi$_2$S$_3$@TiO$_2$ NTAs.

TOC figure
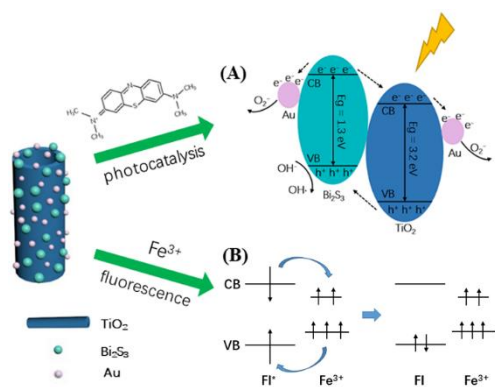
Supporting Information

TiO$_2$ nanotube arrays decorated with Au and Bi$_2$S$_3$ nanoparticles for efficient Fe^{3+} ions detection and dye photocatalytic degradation

Jianying Huang [1], Jiali Shen [1,2], Shuhui Li [1,3], Jingsheng Cai [2], Shanchi Wang [2], Yao Lu [3], Jihuan He [2], Claire J. Carmalt [3], Ivan P. Parkin [3], Yuekun Lai [1*]

[1] *College of Chemical Engineering, Fuzhou University, Fuzhou 350116, PR China*

[2] *National Engineering Laboratory for Modern Silk, College of Textile and Clothing Engineering, Soochow University, Suzhou 215123, PR China*

[3] *Materials Chemistry Research Centre, Department of Chemistry, University College London, London, UK*

∗ Corresponding author. Prof. Yuekun Lai; Tel.: +86 59122865220.

E-mail address: yklai@fzu.edu.cn (Y.K. Lai).

Figure Captions:

Figure S1. SEM images of Au/Bi$_2$S$_3$@TiO$_2$ NTAs with two concentrations of Au NPs solutions 0.02 wt% (a) 0.005 wt% (b), which all include 500 μl deionized water containing 3.0 mg of thioacetamide and 3.86 mg of bismuth acetate and the mixture was granted to react at 80 °C for 10 hours in the oven.

Figure S2. TEM (a) and HRTEM (b-d) images of Au/Bi$_2$S$_3$ NPs solution.

Figure S3. XRD patterns of the pristine TiO$_2$ NTAs, Au/Bi$_2$S$_3$@TiO$_2$ NTAs, Au@TiO$_2$ NTAs, Bi$_2$S$_3$@TiO$_2$ NTAs.

Figure S4. The samples of photocurrent response (a), photofluorescence spectra excited at 380 nm (b), the UV-Vis diffuse reflectance absorption spectra (c).
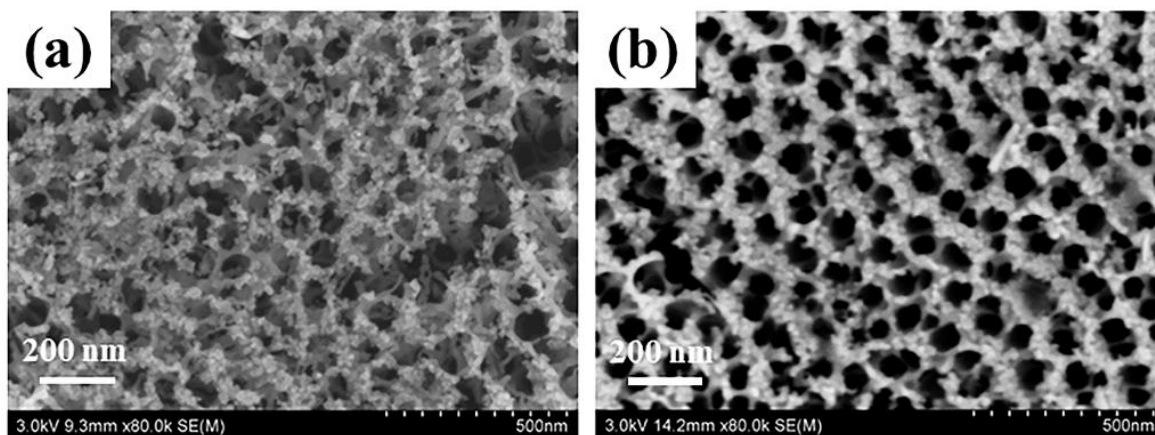
Figure S1. SEM images of Au/Bi$_2$S$_3$@TiO$_2$ NTAs with two concentrations of Au NPs solutions 0.02 wt% (a) 0.005 wt% (b), which all include 500 μl deionized water containing 3.0 mg of thioacetamide and 3.86 mg of bismuth acetate and the mixture was granted to react at 80 °C for 10 hours in the oven.
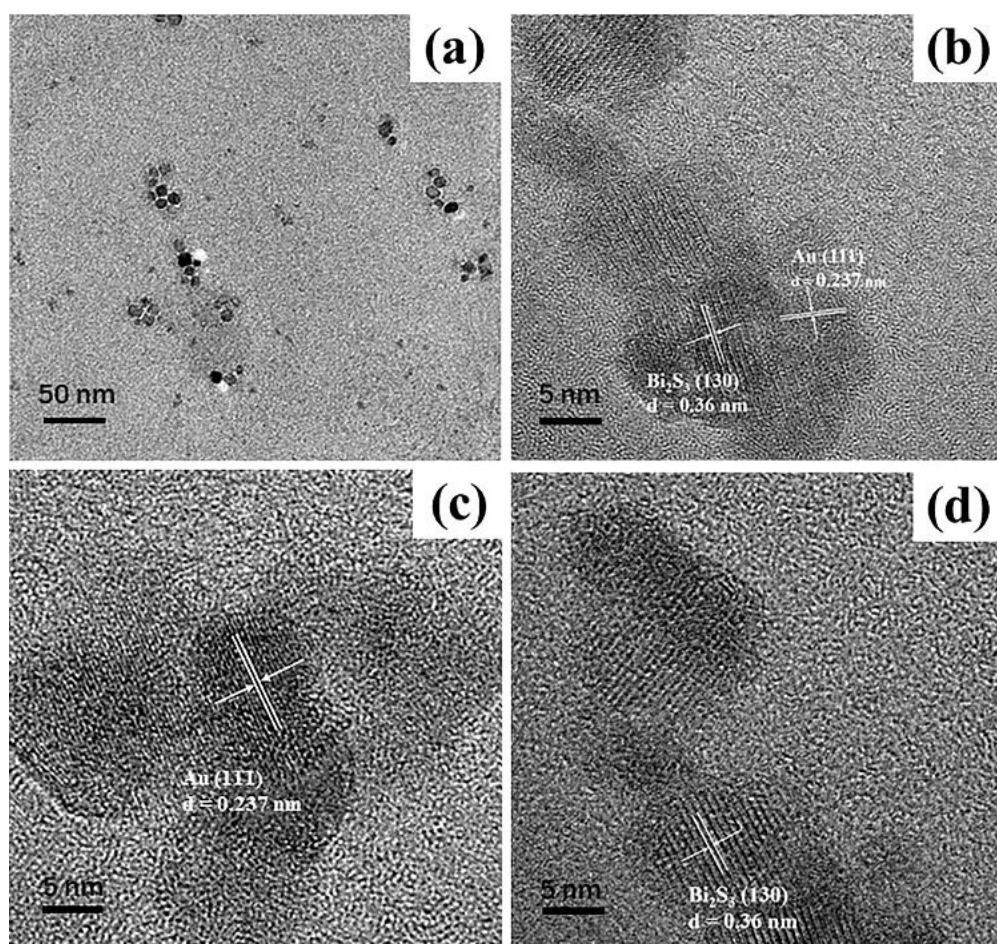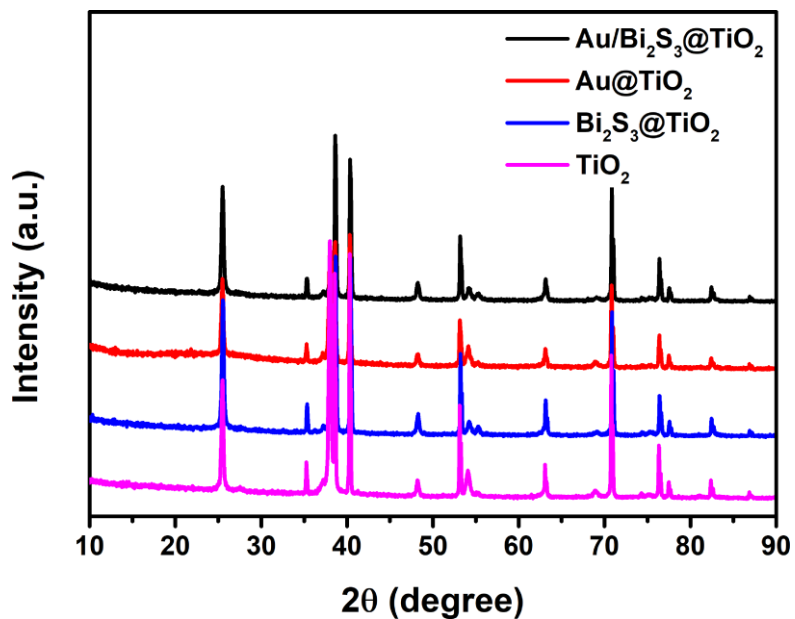

Figure S2. TEM (a) and HRTEM (b-d) images of Au/Bi$_2$S$_3$ NPs solution.

Figure S3. XRD patterns of the pristine TiO_2 NTAs, $Au/Bi_2S_3@TiO_2$ NTAs, $Au@TiO_2$ NTAs, $Bi_2S_3@TiO_2$ NTAs.
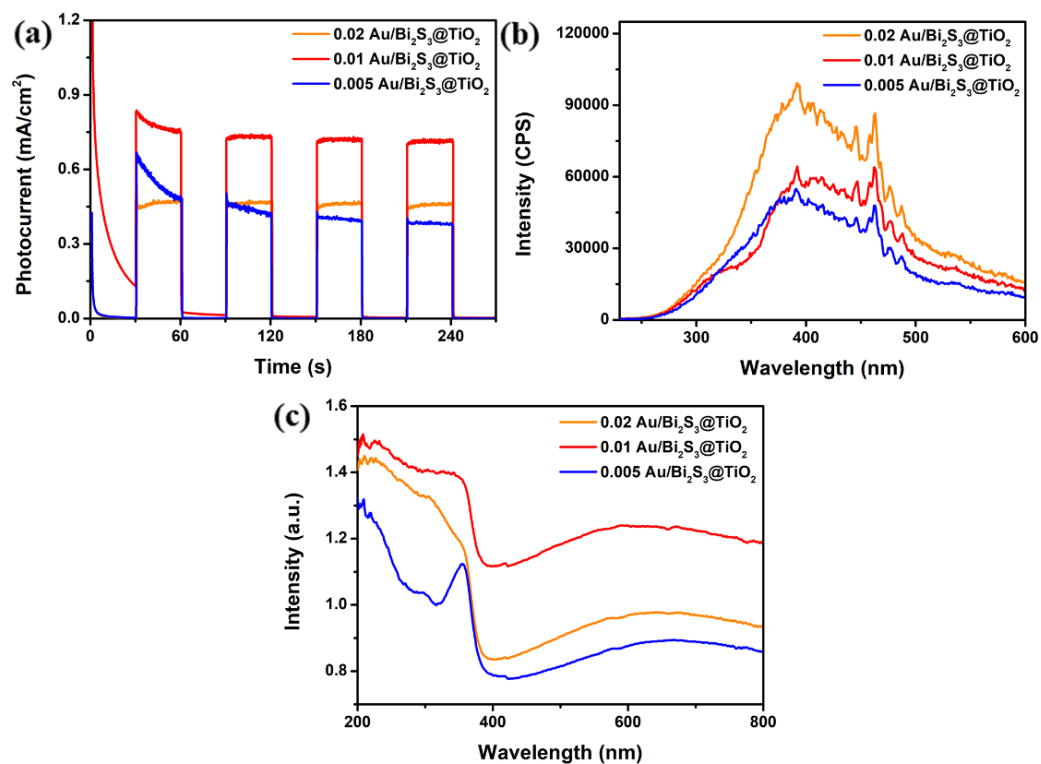

Figure S4. The samples of photocurrent response (a), photofluorescence spectra excited at 380 nm (b), the UV-Vis diffuse reflectance absorption spectra (c).